Catalysis Science & Technology

ROYAL SOCIETY OF CHEMISTRY

PAPER

View Article Online
View Journal | View Issue

Cite this: *Catal. Sci. Technol.*, 2026, **16**, 2170

Ethylene oligomerization under confinement using supported Cr(II) and Cr(III) catalysts†

Somnath Bhattacharya, [a] Marc Högler,[b] Johanna R. Bruckner, [c] Boshra Atwi,[a] Matthias Bauer,[d] Niels Hansen,[b] Felix R. Fischer*[d] and Michael R. Buchmeiser *[a]

Supported Cr(II) and Cr(III) catalysts have emerged as versatile systems for the selective oligomerization of ethylene, offering advantages such as easy separation, catalyst recyclability, and reduced polymer formation. However, their performance can be significantly influenced by factors such as pore confinement, active site accessibility, and metal–support interactions, which leads to an altered selectivity as compared to their homogeneous counterparts. Herein, to better understand and potentially overcome these limitations, we investigated how support morphology and confinement influence the behavior of immobilized Cr catalysts during ethylene oligomerization. Supported catalysts were prepared by selective immobilization of the Cr(III) complexes [1-methyl-3-(2-amido-*N*-(2,6-diisopropylpheny-1-yl)phen-1-ylimidazol-2-ylidene)$_2$Cr$_2$-(μ-Cl)$_4$] (**Cr1**), [1-methyl-3-(2-amido-*N*-(2,6-diisopropylpheny-1-yl)phen-1-ylimidazol-2-ylidene)Cr(benzyl)$_2$(THF)] (**Cr2**), and the Cr(II) complex [(CAAC)$_2$CrCl$_2$] (**Cr3**, CAAC = 1-(2,6-diisopropylpheny-1-yl)-3,3,5,5-tetramethyltetrahydropyrrol-2-ylidene), which are all non-selective for ethylene oligomerization in solution, inside the mesopores of ordered mesoporous silica (OMS) materials with varying pore sizes (**OMS$_{66Å}$**, **OMS$_{57Å}$**, **OMS$_{28Å}$**), as well as amorphous silica (**Si60**). The activity and selectivity of the supported catalysts were assessed in comparison to the parent homogenous catalysts. In the presence of methylalumoxane (MAO) as cocatalyst, the immobilized catalysts exhibited lower catalytic activity (0.1–3.1 kg mol Cr^{-1} h^{-1} bar^{-1}) compared to the homogeneous catalysts (6.9–8.3 kg mol Cr^{-1} h^{-1} bar^{-1}), yet with significant reduction in polyethylene (PE) byproduct formation. Upon activation with MAO, particularly the OMS-immobilized catalyst **Cr1@OMS$_{28Å}$** as well as **Cr2@OMS$_{28Å}$** allowed for the selective synthesis of linear α-olefins (LAOs) ≤ C$_{12}$.

Received 5th December 2025,
Accepted 14th February 2026

DOI: 10.1039/d5cy01483b

rsc.li/catalysis

Introduction

Linear α-olefins (LAOs) are highly valuable building blocks due to their use as commodity chemicals in a variety of applications, *i.e.*, comonomers for the production of linear low-density polyethylene (LLDPE) and high-density polyethylene HDPE (α-C$_4$–C$_8$), plasticizer alcohols (α-C$_6$–C$_{10}$), surfactant/detergent alcohols (α-C$_{10}$–C$_{20}$), and synthetic lubricants (α-C$_{14+}$).[1] The synthesis of LAOs is accomplished by the oligomerization of ethylene. The burgeoning interest in the industrial large-scale oligomerization of ethylene into highly valuable short chain LAOs, particularly 1-hexene and 1-octene, has led to the development of a wide range of chromium-based[2–9] catalytic systems over the past decade. As shown in Scheme 1, a generalized mechanism involving

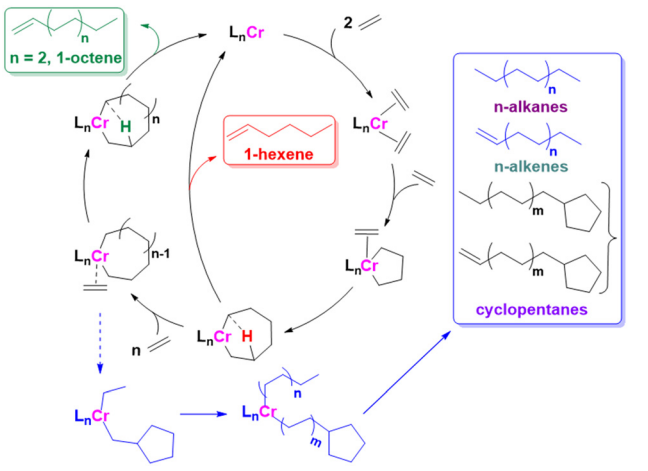

Scheme 1 Ethylene oligomerization *via* the metallacyclic mechanism.[3,10,11]

[a] *Institute of Polymer Chemistry, University of Stuttgart, Stuttgart D-70569, Germany. E-mail: michael.buchmeiser@ipoc.uni-stuttgart.de*
[b] *Institute of Thermodynamics and Thermal Process Engineering, University of Stuttgart, Stuttgart D-70569, Germany*
[c] *Institute of Physical Chemistry, University of Stuttgart, Stuttgart D-70569, Germany*
[d] *Department of Chemistry and Center for Sustainable Systems Design (CSSD), University of Paderborn, Paderborn D-33098, Germany. E-mail: felix.richard.fischer@uni-paderborn.de*

† An unformatted preprint of the present work was deposited on ChemRxiv.[87]

association, ethylene insertion and coordination (oxidative coupling), followed by a reductive elimination (termination) process is postulated for the selective formation of 1-hexene and/or 1-octene.[3,10,11] Alkyl- and alkenyl cyclopentanes have also been observed to form through tetramerization catalysts, with the crucial seven-membered metallacycle being a key intermediate.[10,11]

However, tuning the C_6/C_8 selectivity of Cr-catalyzed oligomerization of ethylene still remains a central topic in this area. In this aspect, attention so far focused mostly on homogeneous Cr-based systems owing to their high activity,[12–14] great selectivity,[11,15–19] diversity of ligand structures,[19] well defined reactive centers,[20] and established reaction mechanism.[20] Despite these advantages, Cr-based homogeneous catalysts still suffer from several drawbacks. For example, examples for highly C_8-selective catalysts with high product purity (>99%) still remain scarce.[9] Additionally, homogeneous Cr-based catalysts often possess low temperature stability and are prone to deactivation.[21] As a result, these catalysts suffer from the complexity of the catalytic process.

Heterogeneous Cr-based catalysts receive increasing academic and industrial interest due to easy and convenient recovery of the catalyst as well as the simple purification of the product through facile filtration of solid catalysts.[22] While homogeneous Cr-based catalysts in ethylene oligomerization have been extensively documented in the literature, heterogeneous systems are still evolving. Representative examples include catalysts immobilized on siliceous or polymeric supports,[23,24] dispersed in ionic liquids,[25–27] and Cr-containing metal–organic frameworks (MOFs).[28,29] Moreover, most of the existing heterogeneous oligomerization systems utilize silica-supported chromium complexes, with selected examples illustrated in Fig. 1A.

Scientists from British Petroleum developed a diverse $CrCl_3(THF)_3$/PNP system (PNP = bis(phosphanyl)amine) on a MAO-modified SiO_2 substrate yielding hexenes with a selectivity of 86% while also minimizing the formation of polymers (Fig. 1, **A**).[30] $Cr[N(SiMe_3)_2]$ and tri*iso*butylalumoxane grafted on silica afford an ethylene trimerization catalyst, although some polymer was still generated with the heterogeneous system (Fig. 1, **B**).[31] Weckhuysen and co-workers have reported on the TAC–Cr^{3+}/SiO_2 complexes (TAC = 1,3,5-tribenzylhexahydro-1,3,5-triazine) that displayed high activity and selectivity in ethylene trimerization (Fig. 1, **C**).[32] Jiang *et al.* synthesized a $Cr(acac)_3$/PNP catalyst, supported onto MAO-modified SBA-15 and evaluated its ethylene oligomerization/polymerization activity (Fig. 1, **D**).[33] Recently, Mohamadnia and co-workers investigated the ethylene trimerization activity and selectivity of Cr-SNS/MMAO catalysts (SNS = bis(2-alkylsulfanyl-ethyl)amine) immobilized on titanium-modified SBA-15 (Fig. 1, **E**).[34]

We recently developed the concept of confinement-governed olefin-metathesis-based selective macro(mono) cyclization[35–38] and Rh-catalyzed *Z*-selective hydrosilylation[39] and hydroboration[40] of alkynes by utilizing catalysts selectively immobilized inside the mesopores of ordered mesoporous silica (OMS) materials including SBA-15.

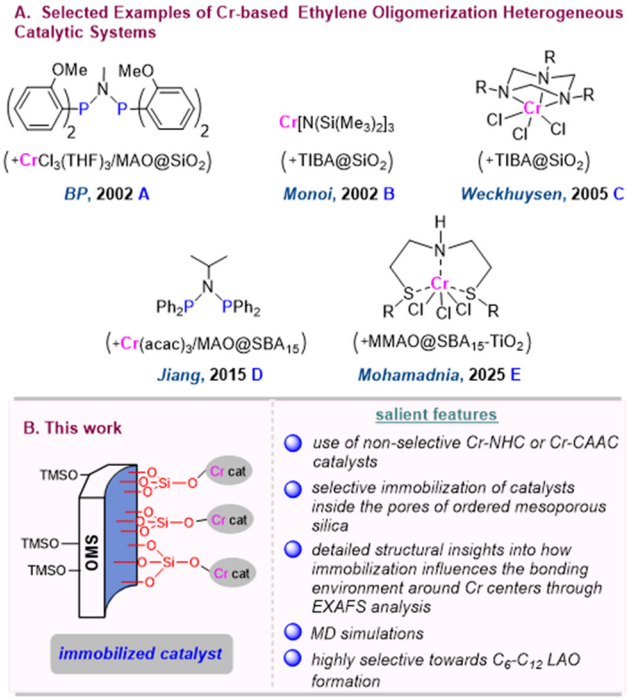

Fig. 1 A) Selected examples of chromium-based heterogeneous ethylene oligomerization catalytic systems; B) focus of this work.

Based on these benchmark results, we were intrigued by the question whether confinement could also be used to suppress the formation of higher oligomers and of poly(ethylene) (PE) in the Cr-catalyzed oligomerization of ethylene using otherwise non-selective catalysts. We also reported on various Cr(II) and Cr(III) catalysts bearing *N*-chelating NHC, phosphino-NHC and CAAC ligands and evaluated their non-selective behavior in ethylene oligomerization/polymerization.[41] These catalysts did not show any selectivity towards LAOs $< C_{24}$ in solution, additionally, extensive formation of PE was observed. Here we report on ethylene oligomerization studies with supported Cr(II) and Cr(III) catalysts selectively immobilized inside different OMS materials (Fig. 1B).

Results and discussion

Catalysts synthesis

As outlined in Fig. 2A, we explored the potential of 1-methyl-3-(2-(2,6-diisopropylphen-1-yl)aminopheny-1-yl)imidazolium iodide (**L1** (ref. 41, 42)) as pro-ligand that provides a simple route to bidentate *N*-chelating NHC. Ligand **L2** was also utilized as a precursor for the synthesis of CAAC.[43] In view of our interest in the catalytic oligomerization of ethylene, complexes **Cr1–Cr3** were synthesized according to published procedures based on a *N*-chelating *N*-heterocyclic carbene (**L1**) and a cyclic alkylamino carbene (CAAC) (**L2**) ligand.[41,44]

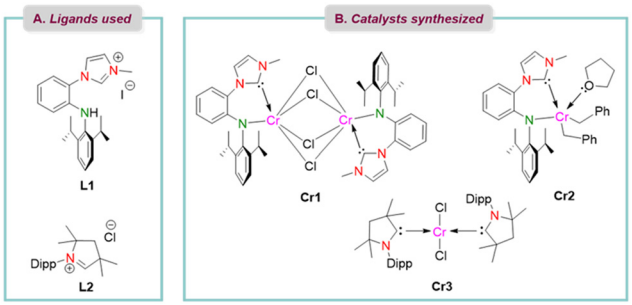

Fig. 2 Chemical structures of A) ligands **L1** and **L2**; B) catalysts **Cr1**–**Cr3** used in this study.

Selective immobilization of catalysts inside the pores of OMS

Supported Cr-catalysts have been reported recently.[33,45,46] Our lab has recently become interested in the pore-selective immobilization of organometallic catalysts inside the mesopores of tailored silica materials and their confinement-governed reactivity.[35–37] Four different silica-based supports with different pore sizes were used; these were three ordered mesoporous silica (OMS) materials with an average pore diameter of 2.8 nm, 5.7 nm and 6.6 nm, referred to as **OMS$_{28Å}$**, **OMS$_{57Å}$** and **OMS$_{66Å}$**, as well as amorphous spherical silica 40–63 μm in size having a broad pore size distribution between 2.1 and 8.0 nm, referred to as **Si60**. Complexes **Cr1**–**Cr3** were used for immobilization (Scheme 2). Pore-selective immobilization was accomplished following a protocol described earlier (see experimental section for more information on the modification these materials).[35,36,47] Briefly, the mesoporous materials were filled with a terpolymer (Pluronic® P-123) followed by functionalization of the outer surface with trimethylsilyl groups using hexamethyldisilazane (HMDS). After removal of the Pluronic® with ethanol, solutions of the Cr-catalyst in toluene were introduced into OMS to yield **cat@OMS$_{66Å}$**, **cat@OMS$_{57Å}$** and **cat@OMS$_{28Å}$**, respectively (Scheme 2).

Characterization of the supported catalysts

The properties of the silica materials and the silica-supported catalysts are presented in Table 1. Distinct differences can be observed in the chromium contents of the silica-supported catalysts **cat@OMS$_{66Å}$**, **cat@OMS$_{57Å}$**, **cat@OMS$_{28Å}$** and **cat@Si60**. Thus, Cr-loadings as determined by inductively-coupled plasma-optical emission spectroscopy (ICP-OES) were 245, 162 and 52 μmol g^{-1} for **Cr1@Si60**, **Cr1@OMS$_{66Å}$** and **Cr1@OMS$_{28Å}$**, respectively (Table 1, entries 2, 7 and 10; S1, SI). In general, higher Cr-loading were observed with **Si60** in comparison to **OMS$_{66Å}$**, **OMS$_{57Å}$** or **OMS$_{28Å}$**, since with **Si60**

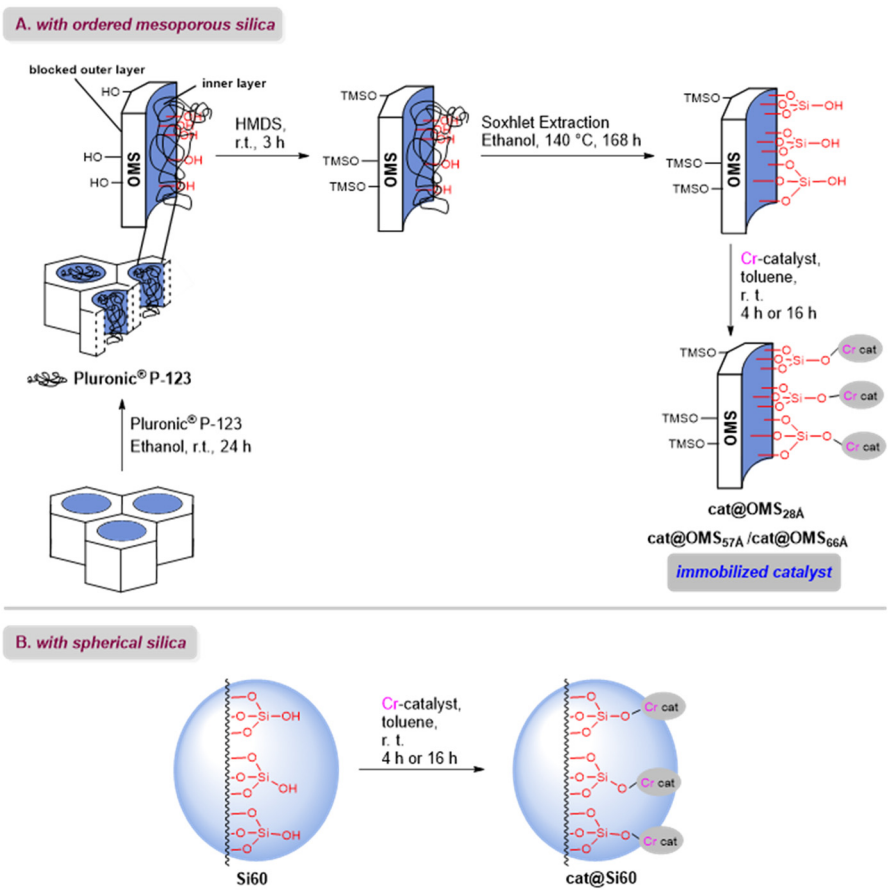

Scheme 2 Pore-selective immobilization of catalysts.

Table 1 Properties of silica and silica-supported catalysts

#	Samples	Cr-content[a] [μmol g^{-1}]	σ_{NLDFT}[b] [m^2 g^{-1}]	V_p[c] [cm^3 g^{-1}]	d_p[d] [nm]
1	$OMS_{28Å}$	—	503	0.36	2.8
2	$Cr1@OMS_{28Å}$	52	534	0.41	2.6
3	$Cr2@OMS_{28Å}$	59	556	0.44	3.2
4	$Cr3@OMS_{28Å}$	71	393	0.31	2.6
5	$OMS_{57Å}$	—	224	0.38	5.7
6	$OMS_{66Å}$	—	322	0.58	6.6
7	$Cr1@OMS_{66Å}$	162	199	0.33	6.1
8	$Cr2@OMS_{57Å}$	178	217	0.30	5.5
9	$Cr3@OMS_{66Å}$	162	251	0.41	6.1
10	Cr1@Si60	245	—	—	—

[a] Determined by ICP-OES. [b] σ_{NLDFT} = surface area obtained using N_2-physisorption (NLDFT equilibrium model). [c] V_P = pore volume obtained using NLDFT equilibrium model. [d] d_P = pore diameter obtained using NLDFT equilibrium model.

the catalyst is not immobilized selectively, utilizing the entire specific surface area of the support.

The immobilized catalysts along with the parent silica materials were analyzed using N_2-physisorption measurements and the resulting textural/surface properties are summarized in Table 1. N_2-sorption isotherms of the pure support and the synthesized silica-supported catalysts are shown in Fig. S9–S11, while the pore-size distributions (determined from N_2-sorption isotherms at 77 K and non-linear density functional theory calculations based on the assumption of cylindrical pores) are depicted in Fig. 3. The **$OMS_{28Å}$**-based materials exhibit completely reversible type IVb isotherms, which is characteristic of cylindrical mesopores ≤ 4 nm. The materials based on **$OMS_{57Å}$** and **$OMS_{66Å}$** give rise to type IVb isotherms, with a uniform H1-type hysteresis loop at a relative pressure (P/P_0) range of 0.4–0.6 with highly parallel adsorption/desorption branches, indicative of uniform and cylindrical mesopores > 4 nm (Fig. S9–S11).[48]

As can be seen from Table 1, in general, **cat@$OMS_{28Å}$** materials showed average pore diameters of 2.6–3.2 nm (Table 1, entries 2–4), which are comparable to the pore diameter of the solid support **$OMS_{28Å}$** of 2.8 nm (Table 1, entry 1). For **$Cr3@OMS_{28Å}$**, the proportional decrease in the pore diameter (d_p), surface area (σ_{NLDFT}) and pore volume (V_p) are in line with a successful immobilization of the catalyst within the mesoporous structure (Table 1, entry 4). As a result, the pore size distribution became broader, which is also evident from Fig. 3a.

$Cr2@OMS_{28Å}$ displayed a slight increase in σ_{NLDFT}, V_p, and d_p (Table 1, entry 3), the latter being a result of the broadening of the pore size distribution. For **$Cr1@OMS_{28Å}$**, a slight reduction in d_p alongside with an increase in both σ_{NLDFT} and V_p was observed (Table 1, entry 2). While **$OMS_{66Å}$** had a pore diameter of 6.6 nm (Table 1, entry 6), the immobilized catalysts **cat@$OMS_{66Å}$** experienced a partial decrease in d_p, leading to a concomitant decrease in σ_{NLDFT} and V_p (Table 1, entries 7 and 9). This is in line with catalysts predominantly immobilized inside the larger mesopores. Similarly, the immobilized catalysts **$Cr2@OMS_{57Å}$** displayed a slightly reduced d_p of 5.5 nm (Table 1, entry 8) when compared to its solid support **$OMS_{57Å}$**, which had a d_p of 5.7 nm (Table 1, entry 5).

Identification of the local coordination structure *via* XAS analysis

XAS (X-ray absorption spectroscopy) can be applied independent of the state of aggregation of the analyzed matter and is therefore tolerant to nearly every experimental condition.[49] XAS is ideally suited to obtain electronic and geometric structure information about complexes in solution

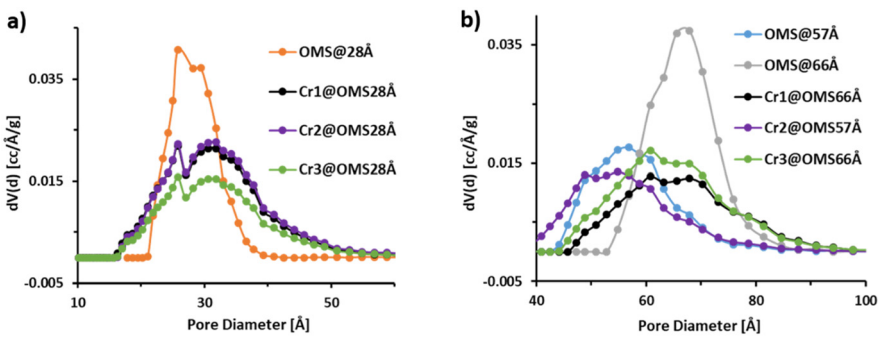

Fig. 3 Pore size distributions of a) **$OMS_{28Å}$**, **$Cr1@OMS_{28Å}$**, **$Cr2@OMS_{28Å}$**, and **$Cr3@OMS_{28Å}$**; b) **$OMS_{57Å}$**, **$OMS_{66Å}$**, **$Cr1@OMS_{66Å}$**, **$Cr2@OMS_{57Å}$**, and **$Cr3@OMS_{66Å}$** determined from N_2-sorption isotherms at 77 K and non-linear density functional theory calculations based on the assumption of cylindrical pores.

or immobilized inside mesoporous materials, where the metal complexes lack long range order.[7,50] A comparison of normalized XANES (X-ray absorption near edge structure) spectra for **Cr1@OMS$_{66Å}$**, **Cr2@OMS$_{57Å}$** and **Cr3@OMS$_{66Å}$** and their homogeneous analogues **Cr1**, **Cr2** and **Cr3** as well as the MAO-activated species of **Cr3** (**Cr3_MAO activated**) is shown in Fig. 4. The pre-edge region in the XANES spectra of metal complexes originates from 1s-electron transitions into the lowest unoccupied molecular orbitals (LUMOs). For transition metal complexes with incomplete (*n*-1)d-electron set, these pre-edge features typically exhibit notable contributions from unoccupied metal (*n*-1)d-orbitals and provide structural insights into their coordination geometry.[49,51,52] Additionally, pre-peak- and absorption edge energies correlate with the electron density of the excited atom and consequently its oxidation state.[49]

XAS-investigation of the immobilized complexes

Pre-edge- and absorption edge energies of **Cr1@OMS$_{66Å}$**, **Cr2@OMS$_{57Å}$** and **Cr3@OMS$_{66Å}$** were comparable and found in the range of 6000.7 to 6001.3 eV (Table S2). Comparison of the XANES spectra of **Cr2@OMS$_{57Å}$** and **Cr3@OMS$_{66Å}$** with those of the solid references revealed pronounced changes in the pre-edge fine structure together with edge shifts, whereas only minor deviations were observed after the immobilization of **Cr1**. Since Cr-XANES spectra are highly sensitive towards variations in the primary ligand environment,[53–56] this pattern suggests modifications of the bonding motif upon immobilization of **Cr2** and **Cr3** but only modest structural changes for **Cr1**. Those observations were further underlined by comparing the Fourier-transformed (FT)-EXAFS (extended X-ray absorption fine structure) functions of the immobilized and homogeneous complexes (Fig. 5).

In general, the *k*-spaces for calculating the FT-functions of the immobilized samples were slightly smaller than those for the homogeneous analogues resulting in a reduced resolution of the corresponding FT-data (see detailed information about EXAFS-analysis in the SI). After immobilization of **Cr1**, the two first-shell features of the homogeneous complex (Fig. 5a, red trace) coalesce into a single peak for the immobilized sample without evidence for a change in coordination number (Fig. 5a, black trace). In contrast, immobilization of **Cr2** leads to an increased first-shell FT amplitude consistent with a higher number of coordinating donor atoms (Fig. 5b, black trace). For **Cr3**, immobilization is accompanied by a pronounced contraction of the Cr-donor distances, as evidenced by a shift of the first-shell FT peak to shorter distances (Fig. 5c, black trace).

Detailed structural information about the effect of immobilization on the bonding situation around the Cr centers were gained by EXAFS fitting (Table 2). For full sets of scattering paths, see Table S4. The contributions of heavy Si-back scatterers in those EXAFS-fits are either represented by single Si- or multiple Si–O-scattering paths (Table S4). Since the distances between Si back scatterers and chromium centers overlap with the distances of lighter atoms in the backbone of the organic ligands, the degeneracies for Si single scattering paths might not represent the actual

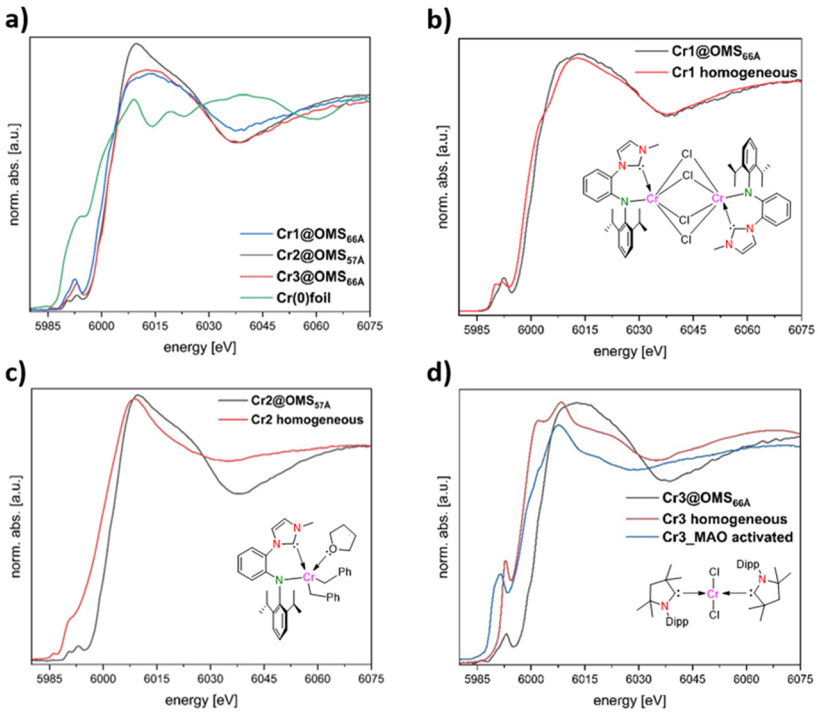

Fig. 4 a) XANES spectra of **Cr1(III)@OMS$_{66Å}$** (blue), **Cr2(III)@OMS$_{57Å}$** (black), **Cr3(II)@OMS$_{66Å}$** (red) and **Cr(0) foil** (green); b) **Cr1(III)@OMS$_{66Å}$** *vs.* **Cr1(III)**; c) **Cr2(III)@OMS$_{57Å}$** *vs.* **Cr2(III)**; d) **Cr3(II)@OMS$_{66Å}$** *vs.* **Cr3(II)** *vs.* **Cr3(II)_MAO activated**.

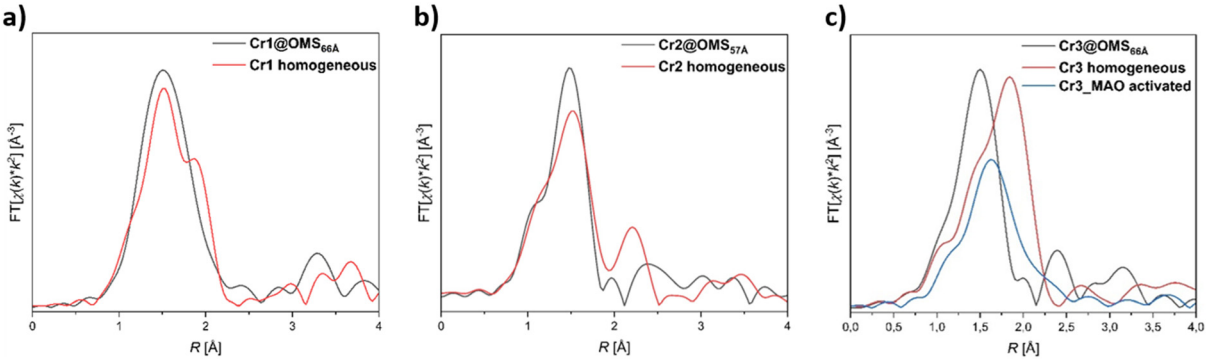

Fig. 5 Comparison of the FT–EXAFS spectra of immobilized Cr(II/III) complexes and their homogeneous analogues: a) **Cr1@OMS$_{66Å}$** *vs.* **Cr1**; b) **Cr2@OMS$_{57Å}$** *vs.* **Cr2**; c) **Cr3@OMS$_{66Å}$** *vs.* **Cr3** *vs.* **Cr3_MAO activated**. Spectra are plotted without element- and path-specific phase shifts.

number of Si-based back scatterers in the respective distance. $S_0{}^2$- and delE_0 values are collected in Table S3 (SI).

EXAFS analysis of **Cr1@OMS$_{66Å}$** confirms the conservation of the dimeric structure after immobilization of the homogeneous reference **Cr1**.[41] However, the number of first-shell chloride back scatterers decreases from four in the homogeneous complex to three within the OMS material. The C- and N-donor atoms of the bidentate NHC ligand are furthermore modeled as a single Cr–N/C scattering path because carbon and nitrogen exhibit very similar backscattering amplitudes complicating the reliable separation of their individual contributions by EXAFS. The degeneracy for this path, N = 2.3(1) (Table 2), lies at the upper bound of a purely two-donor assignment that could indicate a mixture of two different chromium environments. Taken together with three chloride scatterers and the preserved dimeric motif in the pores, the most plausible structure for **Cr1@OMS$_{66Å}$** is an asymmetrically coordinated chromium dimer comprising one pentacoordinate and one hexacoordinate center with the latter anchoring to the pore wall *via* a Si–O-linker (Fig. 6a). Such asymmetric coordination geometries for Cr-dimers have already been reported in the literature.[57]

Table 2 First shell coordination numbers (N), bond lengths (R + ΔR) and Debye–Waller factors (σ^2) of **Cr1@OMS$_{66Å}$**, **Cr2@OMS$_{57Å}$**, **Cr3@OMS$_{66Å}$** and Cr3_MAO activated

Scattering paths	Cr1@OMS$_{66Å}$		
	N	R + ΔR [Å]	σ^2 [Å^2]
Cr–N	2.3(1)	1.947(7)	0.0029(4)
Cr–Cl	1.7(1)	2.247(9)	0.0082(5)
Cr–Cl	1.4(1)	2.782(15)	0.0089(6)
Cr–Cr	0.9(1)	3.134(53)	0.0106(41)
Scattering paths	Cr2@OMS$_{57Å}$		
	N	R + ΔR [Å]	σ^2 [Å^2]
Cr–C	2.8(1)	2.003(3)	0.0020(3)
Cr–N	1.7(1)	2.149(11)	0.0077(13)
Cr–O	1.1(1)	2.409(10)	0.0024(14)
Scattering paths	Cr3@OMS$_{66Å}$		
	N	R + ΔR [Å]	σ^2 [Å^2]
Cr–O	1.9(1)	1.950(7)	0.0022(12)
Cr–C	1.7(1)	2.090(34)	0.0049(12)
Scattering paths	Cr3_MAO activated		
	N	R + ΔR [Å]	σ^2 [Å^2]
Cr–C	3.0(1)	2.108(15)	0.0044(11)
Cr–Cl	0.7(1)	2.338(24)	0.0067(21)

Similar results were observed for **Cr2@OMS$_{57Å}$**. Upon successful immobilization, the substitution of one or both benzyl ligands in **Cr2** by surface-bound Si–O-groups was expected. This scenario would be consistent with the observed pronounced shift of the absorption edge to higher energy (Fig. 4c), as replacement of one or two strong σ-donor ligands by weaker, highly electronegative oxygen-donors decreases electron density at the chromium centers. Because carbon and oxygen have similar backscattering amplitudes, EXAFS could not reliably resolve whether one or both benzyl ligands were substituted during immobilization. Whereas the experimental EXAFS data of the homogeneous precursor **Cr2** are fitted best by applying a coordination number of N = 5.1(3) (N = 1.0(1) + 2.9(1) + 1.2(1)), (SI, Table S4), the immobilized material, however, exhibits an apparent average coordination number of N = 5.6(3) suggesting a mixture of penta- and hexacoordinate chromium environments. This interpretation is further supported by the distinct change in the pre-edge pattern between **Cr2** and **Cr2@OMS$_{57Å}$**, indicative of a substantial geometric reorganization upon immobilization. The pre-edge fine structure of **Cr2@OMS$_{57Å}$** closely resembles that of octahedral, oxygen-coordinated chromium species – *e.g.* Cr_2O_3, $Cr(OH)_3$ or $Cr(acac)_3$ – and suggests the formation of a significant fraction of a hexacoordinate chromium–oxide by-product during the immobilization of **Cr2** (Fig. 6b).[53,58] Formation of this oxide species might explain the pronounced loss of catalytic activity upon immobilizing **Cr2** in **OMS$_{57Å}$** material – from 8.3 kg(product) mol Cr^{-1} h^{-1} bar^{-1} under homogeneous conditions to 0.7 kg(product) mol Cr^{-1} h^{-1} bar^{-1} in **OMS$_{57Å}$** – representing the largest decline observed among the immobilized catalysts (*vide infra*, Table 3).

The experimental EXAFS data for **Cr3@OMS$_{66Å}$** are best reproduced by replacing both chloride ligands in **Cr3** with

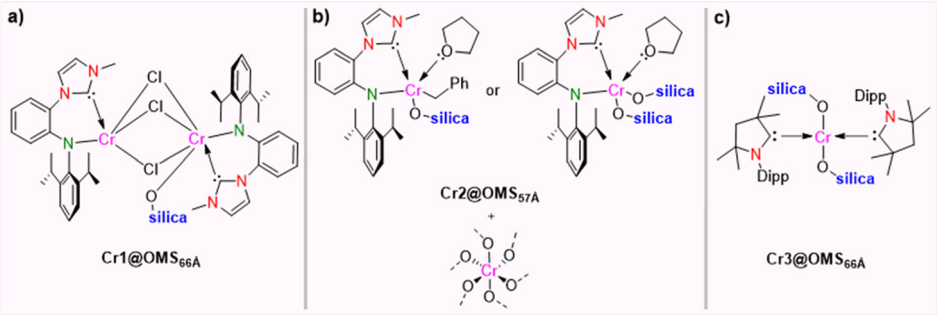

Fig. 6 Proposed structures for the immobilized Cr complexes a) **Cr1@OMS$_{66Å}$**, b) **Cr2@OMS$_{57Å}$** and c) **Cr3@OMS$_{66Å}$** based on XAS analysis. Regarding **Cr2@OMS$_{57Å}$**, the hexacoordinate chromium oxide species could not be characterized further and is therefore shown only schematically.

Table 3 Ethylene oligomerization results for complexes **Cr1**–**Cr3** using MAO as cocatalyst

		LAOs (wt%)[e,f]								
#	Catalyst	C_6	C_8	C_{10}	C_{12}	C_{14}	$>C_{14+}$	PE (mg)	Activity[g]	T_m (°C)[h]
1	Cr1[a]	3	7	11	13	14	52	176	8.1	117
2	Cr1@Si60[b]	10	20	22	18	10	20	71	2.3	131
3	Cr1@OMS$_{66Å}$[b]	4	10	14	17	17	38	37	1.2	133
4	Cr1@OMS$_{28Å}$[b]	15	30	25	25	4	1	3	0.1	—[i]
5	Cr1@OMS$_{28Å}$[c]	18	58	12	12	—	—	—	0.004	—[i]
6	Cr1@OMS$_{28Å}$[d]	24	60	7	9	—	—	—	0.003	—[i]
7	Cr2[a]	4	9	15	17	16	39	251	8.3	131
8	Cr2@Si60[b]	5	10	16	18	14	37	80	2.6	136
9	Cr2@OMS$_{57Å}$[b]	10	14	20	20	13	29	26	0.7	129
10	Cr2@OMS$_{28Å}$[b]	14	24	30	21	8	3	10	0.3	136
11	Cr3[a]	6	15	18	20	16	25	200	6.9	124
12	Cr3@Si60[b]	17	23	15	14	9	22	92	3.1	134
13	Cr3@OMS$_{66Å}$[b]	6	9	12	14	19	40	35	1.2	135
14	Cr3@OMS$_{28Å}$[b]	10	14	19	19	19	29	25	0.9	134

[a] *ca.* 1 mg of cat., 1000 eq. MAO, 10 mL toluene, 80 °C, 10 bar, 2 h. [b] *ca.* 15 mg of immobilized cat., 1000 eq. MAO, 10 mL toluene, 80 °C, 10 bar, 2 h. [c] Oligomerization was performed at 50 °C. [d] Oligomerization was performed at 20 °C. [e] Determined by GC, values of C_4 are not given due to volatility. [f] Average of two experiments. [g] kg(product) mol Cr^{-1} h^{-1} bar^{-1}, determined by adding polymerization activity to oligomerization activity. [h] Determined by DSC. [i] Not determined due to very low yield or no PE produced.

oxygen donors from surface Si–O groups inside the OMS pores (Table 2 and Fig. 6c).[41] This substitution significantly contracts the bond motifs between metal center and first ligand sphere, which is consistent with the FT-EXAFS comparison of **Cr3@OMS$_{66Å}$** and **Cr3** (Fig. 4d)), since two Cr–Cl bonds (2.33 and 2.34 Å) are replaced by two Cr–O bonds having an average fitted length of 1.950(7) Å (Table 2). The combination of chloride/oxygen exchange together with a possible immobilization-induced change in coordination geometry of the chromium complex is assumed to account for the pronounced shift of the absorption edge between **Cr3@OMS$_{66Å}$** and **Cr3** and furthermore align with the changes observed in the pre-edge fine structure (Fig. 4d).[53] Especially, the intensity of the shoulder feature at around 6002 eV (Fig. 4d) is markedly reduced upon immobilization or MAO activation. This shoulder signal represents a characteristic feature of chloride ligands being bound to transition metals and originates from a so-called shakedown-process describing a ligand-to-metal charge transfer (LMCT) after the excitation of a metal-centered 1s electron into metal-centered 4p states.[59–63] The reduction of this shoulder signal upon immobilization or MAO activation underlines the assignment of this feature to Cr–Cl bonding motifs, as chloride ligands are replaced during both immobilization and activation. A similar trend is observed for the immobilization of **Cr1** (Fig. 4b). However, this effect is less pronounced because only one quarter of the coordinating chloride ligands is substituted upon immobilization and the fact that the measured absorption edge energy represents an average over the two Cr centers within the **Cr1** dimer.

XAS-investigation of the MAO-activated Cr3 complex

XAS measurements were also carried out on **Cr3** activated by 150 eq. of MAO. The XANES spectrum of the MAO-activated **Cr3** species exhibits a shift of the absorption edge by around 2 eV toward lower energies, while the fine structure of the edge as well as the energy of the white-line region (the absorption maximum of the edge) remains nearly unaltered

(Fig. 4d and Table S2, SI). Least-squares fitting of the experimental EXAFS data for the MAO-activated **Cr3** species could only be achieved when three carbon-based donor atoms and one chloride anion were included in the first coordination sphere (Scheme 3).

We interpret these XANES- and EXAFS-results as evidence for similar coordination geometries of **Cr3** and **Cr3_MAO activated**, differing only in the identity of the coordinating ligands. The replacement of an electron withdrawing chloride ligand by a strong σ-donating methyl group provides a plausible explanation for the observed energy shift and aligns with the edge shift between the **Cr3** pre-catalyst and its immobilized analogue **Cr3@OMS$_{66Å}$**, in which the chloride ligand is replaced by a less donating and more electronegative siloxide moiety (Fig. 4d and S12, SI). This substitution likely represents the initial step in the activation of **Cr3**, potentially followed by the replacement of the second chloride ligand upon exposure to higher MAO concentrations.[64–67]

To probe the potential formation of a Cr(I)$(C_6H_5CH_3)_2$ sandwich complex, previously reported as a favored deactivation pathway in toluene,[65–68] we compared the XAS data of **Cr3** and **Cr3_MAO activated** with those of Cr(0)$(C_6H_6)_2$ (Table S2 and Fig. S12, SI). As toluene is anticipated to coordinate in an η^6-fashion, the formation of significant amounts of Cr(I)$(C_6H_5CH_3)_2$ would yield a markedly higher signal intensity for the first coordination shell in the FT-EXAFS region, which is not observed (Fig. S12b, SI). Because Cr(0)$(C_6H_6)_2$ and Cr(I)$(C_6H_5CH_3)_2$ are expected to adopt similar coordination geometries, their absorption edge fine structures should be comparable despite the lower d-electron count in Cr(I). Since the XANES-spectrum of Cr(0)$(C_6H_6)_2$ displays an almost featureless edge region, a significant concentration of Cr(I)$(C_6H_5CH_3)_2$ within the MAO-activated **Cr3** solution would result in a pronounced reduction of fine-structure intensity for **Cr3_MAO activated** compared to the **Cr3** pre-catalyst spectrum (Fig. S12a, SI).

Due to the limited signal-to-noise ratio, it remains unclear whether the methyl and chloride ligands act as terminal ligands or as bridging groups forming a bimetallic complex. However, based on our previous EXAFS analysis of a MMAO-activated (PNP)Cr(II)$(Me)_2$ species,[65] we consider the formation of bimetallic species unlikely, given the steric constraints imposed by the two CAAC ligands. Furthermore, the pronounced sensitivity of the Cr K-edge position to variations in both oxidation state and ligand environment currently precludes an unambiguous assignment of the chromium oxidation state under the applied experimental conditions. A more detailed investigation of the structure and oxidation state of the MAO-activated Cr3 pre-catalyst – employing higher MAO excess and complementary XAS, XES, and EPR measurements – to elucidate the complete activation pathway of the Cr-based pre-catalysts mentioned here is part of our ongoing research.

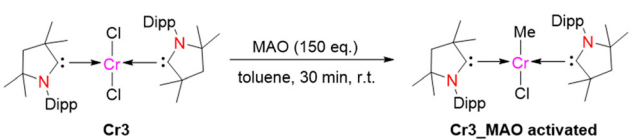

Cr3 Cr3_MAO activated

Scheme 3 Proposed structure of **Cr3** after activation with 150 eq. of MAO.

Ethylene oligomerization studies (homogeneous)

The chromium complexes **Cr1–Cr3** were evaluated as pre-catalysts in the oligomerization of ethylene at 80 °C in toluene at 10 bar ethylene pressure using 1000 eq. of MAO as cocatalyst.[41] Results are compiled in Table 3. In all cases, they proved to be non-selective towards 1-hexene and/or 1-octene, revealing a broad oligomer distribution ranging from C_4 to C_{28} oligomers (for representative GC–MS spectra of the products after catalytic oligomerization using **Cr1**/MAO and **Cr2**/MAO see Fig. S15 and S19, respectively). In most cases, PE was the main product and higher olefins $>C_{12}$ accounted for the majority of the oligomers. All chromium complexes displayed moderate catalytic activity (6.9–8.3 kg mol Cr^{-1} h^{-1} bar^{-1}) in ethylene oligomerization. Noteworthy, activity was determined by adding polymerization activity to oligomerization activity.

Ethylene oligomerization studies (heterogeneous)

Supported Cr-complexes were evaluated in ethylene oligo-/polymerization reaction using the same condition previously used for corresponding homogeneous version.[41] Table 3 summarizes the activities and product/oligomer distributions of the supported Cr-based catalysts. **Cr3@Si60**/MAO [α-C_6–C_{14} (78 wt%) and $>C_{14+}$ (22 wt%)], **Cr3@OMS$_{66Å}$**/MAO [α-C_6–C_{14} (60 wt%) and $>C_{14+}$ (40 wt%)] and **Cr3@OMS$_{28Å}$**/MAO [α-C_6–C_{14} (71 wt%) and $>C_{14+}$ (29 wt%)] exhibited similar selectivity as compared to the homogeneous system **Cr3**/MAO [α-C_6–C_{14} (75 wt%) and $>C_{14+}$ (25 wt%)] though PE formation was significantly reduced particularly with **Cr3@OMS$_{28Å}$**/MAO for which the oligomer distributions also centered more on lighter LAOs (Table 3, entries 11–14). In case of silica-supported activated catalysts **Cr1@Si60**/MAO [α-C_6–C_{14} (80 wt%) and $>C_{14+}$ (20 wt%)] and **Cr1@OMS$_{66Å}$**/MAO [α-C_6–C_{14} (62 wt%) and $>C_{14+}$ (38 wt%)] (Table 3, entries 2 and 3), the oligomer distribution centered on lighter α-olefins fractions in comparison to the homogeneous **Cr1**/MAO system where the distribution was dominated by heavier α-olefins fractions [α-C_6–C_{14} (48 wt%) and $>C_{14+}$ (52 wt%)] (Table 3, entry 1).

The most striking effect was observed with the supported catalyst **Cr1@OMS$_{28Å}$**/MAO. The GC–MS spectrum of the liquid phase products using the **Cr1@OMS$_{28Å}$**/MAO system is shown in Fig. 7 and reveals a narrow oligomer distribution ranging from C_6 to C_{12} oligomers with a sharp increase in selectivity towards lighter α-olefins fractions [α-C_6–C_{14} (99 wt%) and $>C_{14+}$ (1 wt%)] (Table 3, entry 4; Fig. 7 and 8a). A separate, minor distribution of odd-numbered carbon olefins (C_7–C_{13}) was also observed, suggesting that chromium

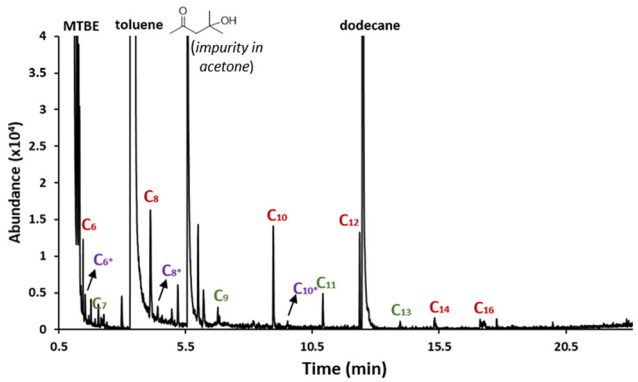

Fig. 7 Representative GC–MS spectrum of the products after catalytic oligomerization using **Cr1@OMS$_{28Å}$**/MAO. Internal standard: *n*-dodecane.

species underwent chain methylation reactions due to residual Me_3Al in the MAO.[69] Similar selectivity was obtained with the **Cr2@OMS$_{28Å}$**/MAO catalyst mostly centered on lighter α-olefins fractions [α-C_6–C_{14} (97 wt%) and >C_{14+} (3 wt%)] (Table 3, entry 10; Fig. 8c and S20, SI). The distribution of oligomeric 1-alkenes with **Cr1**/MAO, **Cr1@Si60**/MAO, **Cr1@OMS$_{66Å}$**/MAO and **Cr1@OMS$_{28Å}$**/MAO is depicted in Fig. 8a. As we transition from the homogenous system to heterogenous system, a distinct correlation of the pore size of the immobilized catalysts with product selectivity can be observed. Thus, the **Cr1@OMS$_{28Å}$**/MAO catalyst with the smallest mesopores demonstrated the ability to preferentially generate lower linear α-olefins up to C_{12} (Fig. 8a).

As expected, immobilization on **Si60** resulted in a more active catalyst compared to the utilization of **OMS$_{66Å}$** and **OMS$_{28Å}$** (Fig. 8b). This finding can be attributed to the typically larger pore size distribution of **Si60** and **OMS$_{66Å}$** in comparison to **OMS$_{28Å}$**, which allows for more efficient transport of ethylene within the material, leading to an improvement in the oligomerization process. The trends that were observed align well with previous reports.[33,46,70]

Since the **Cr1@OMS$_{28Å}$**/MAO system demonstrated enhanced selectivity towards lighter α-olefins fractions [α-C_6–C_{14}], further ethylene oligomerization experiments were performed at varying temperatures to investigate how temperature variations influence the selectivity. The selectivity towards lighter α-olefins fractions [α-C_6–C_{12}] remained constantly high at lower temperatures (see Fig. S17 and S18, SI). Additionally, PE formation was completely suppressed at lower temperatures. A significant enhancement in the selectivity towards C_8 was detected at lower temperatures; the C_8 selectivity rose from 30 to 58 and 60 wt% at 80, 50 and 20 °C, respectively (Table 3, entries 4–6). The increased C_8-selectivity at lower temperature may be attributed to an increased stability of the metallacyclononane[71] intermediate (*vide infra*) as well as a higher ethylene concentration.[14] However, a significant reduction in catalytic activity was noted at lower temperatures (0.004 and 0.003 kg mol Cr^{-1} h^{-1} bar^{-1} at 50 and 20 °C, respectively; Table 3, entries 5 and 6).

Overall, catalysts confined within small mesopores, *i.e.* **Cr1@OMS$_{28Å}$**/MAO and **Cr2@OMS$_{28Å}$**/MAO, show promising selectivity towards LAOs ≤ C_{12} (Fig. 8c). Confinement also strongly minimizes or fully eliminates the undesired formation of PE (Fig. 8c). The minor amounts of PE that form with the immobilized catalysts at 80 °C are probably a result of catalyst leaching. The melting points (T_m) of the obtained PEs were determined by differential scanning calorimetry (DSC); findings are listed in Table 3. DSC analyses indicate that linear, high-density PE (HDPE) is formed using the supported catalysts (Fig. S21–S23); ^1H and ^{13}C measurements on specific PE samples further confirm the formation of HDPE with vinyl end groups (Fig. S7 and S8).

The reduced catalytic activity of the immobilized catalysts may be ascribed to a combination of several factors including the formation of chromium oxide species as suggested by XAS spectroscopy (*vide supra*), changes in the oxidation states of the active sites after immobilization, reduced catalyst dispersion,[70,72,73] restricted accessibility[72] of the cocatalyst MAO to the active sites due to steric hindrance by the pore wall,[73] and a restricted access of ethylene to the active sites,[72] thereby blocking ethylene insertion.[33,46]

Mechanism of ethylene oligomerization using supported catalysts

The mechanism of ethylene oligomerization using the chromium catalysts supported on mesoporous silica may be understood in terms of the metallacyclic mechanism, as

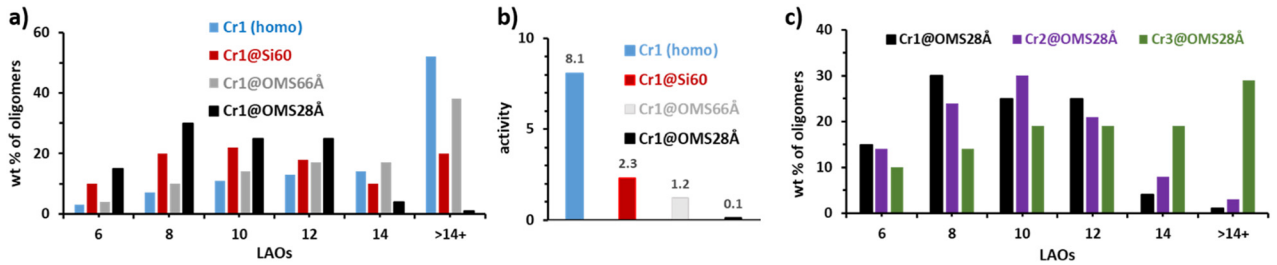

Fig. 8 a) Distribution of oligomeric 1-alkenes with **Cr1**/MAO, **Cr1@Si60**/MAO, **Cr1@OMS$_{66Å}$**/MAO, and **Cr1@OMS$_{28Å}$**/MAO; b) activity in kg(product) mol Cr^{-1} h^{-1} bar^{-1} with **Cr1**/MAO, **Cr1@Si60**/MAO, **Cr1@OMS$_{66Å}$**/MAO, and **Cr1@OMS$_{28Å}$**/MAO in toluene; c) distribution of oligomeric 1-alkenes with **Cr1**–**Cr3@OMS$_{28Å}$**/MAO. For the GC–MS spectrum of **Cr1@OMS$_{28Å}$**/MAO, see Fig. 7.

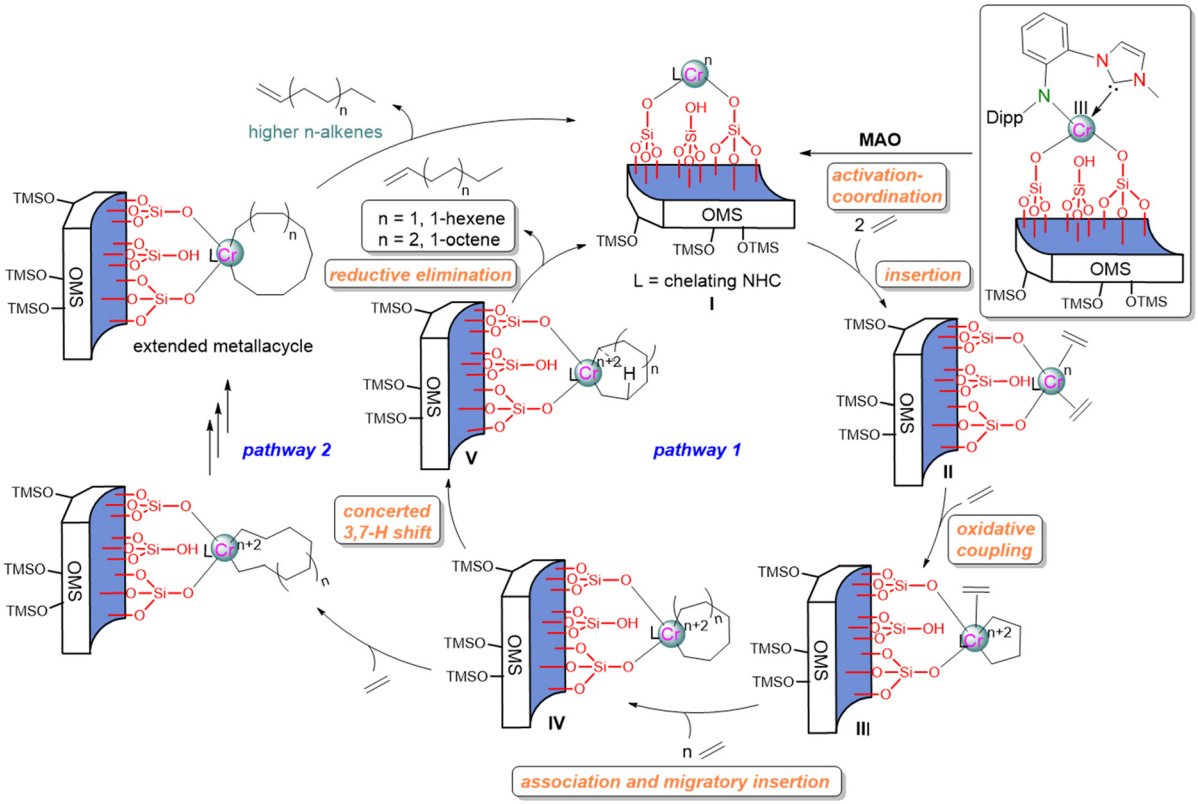

Scheme 4 Schematic representation of the generally accepted metallacyclic pathway for Cr-catalyzed ethylene oligomerization. Complex **Cr2@OMS$_{28Å/66Å}$** was used as representative example.

illustrated in Scheme 4.[74] To prevent any potential overinterpretation, it is important to note that Scheme 4 is presented here for illustrative purposes, primarily to aid in the discussion of how confinement effects influence the catalytic process, rather than to propose a novel mechanism. The catalytic cycle is initiated with the activation of the chromium center in the presence of a cocatalyst (MAO) generating an active Cr species **I** (pathway 1). The active Cr species **I** couples with two ethylene molecules, and undergoes oxidative coupling to form a metallacyclopentane complex **III**. Introducing additional ethylene into the metallacyclopentane **III** results in the larger ring metallacycles **IV**. Further concerted 3,3+2*n*-H shift (n = 1, 2, 3…) leads to the formation of intermediate **V**. Breakdown of the metallacycle proceeds *via* reductive elimination to yield 1-hexene and 1-octene, respectively, and regenerates the active catalytic species **I**. The formation of α-C_{10}–C_{14} olefins can be explained *via* the formation of extended metallacyles from **IV** (Scheme 4, pathway 2). We surmise that two different oligomerization mechanisms can be operative at the same time with two catalytically active chromium sites, one that facilitates the formation of oligomers and the other that drives polyethylene formation.[74,75] The latter is fully suppressed under confinement. Our results align well with reports by Kaphan and co-workers.[76]

Discussion on the confinement effect

Under confinement,[46,77–81] the selective formation of the α-C_6–C_{12} oligomers can also be understood through the metallacyclic mechanism. The restricted pore environment functions as a molecular sieve, facilitating the diffusion of shorter oligomers (α-C_6–C_{12}) in and out of the pores. As the oligomer continues to grow, larger chromacycles face steric strain and diffusion constraints, which selectively destabilize the larger metallacyclic intermediates, leading to early termination of chain growth *via* concerted 3,3+2*n* H-shift/β-hydride elimination. Furthermore, the confined space stabilizes smaller metallacyclic intermediates through surface interactions, while larger metallacycles are destabilized by steric constraints and are thus more prone to termination, thereby limiting the product distribution to ≤C_{12}. Consequently, the confined space preferentially promotes the formation of the shorter oligomers, resulting in a higher selectivity for α-C_6–C_{12} products. This confinement-driven behavior contrasts with Phillips-type Cr catalysts, where small pore sizes promote long-chain polymerization *via* a Cossee–Arlman mechanism, highlighting the mechanistic specificity of metallacycle-mediated oligomerization under confinement.[82]

Molecular dynamics simulations were performed at 80 °C to better understand the effect of the confinement within the ordered mesoporous silica materials and confirm the size-

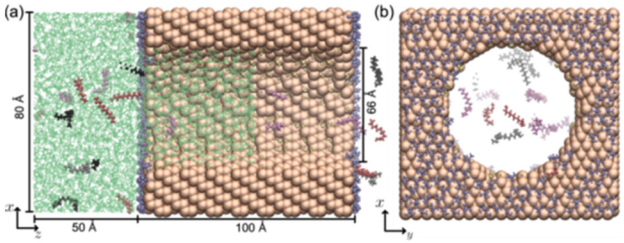

Fig. 9 (a) Side view of the cylindrical pore model with a diameter of 66 Å. The pierced silica block is flanked by two solvent reservoirs (only one is displayed). (b) Front view of the silica block, showing the trimethylsilyl (TMS)-functionalized (111) exterior surface of the β-cristobalite silica. Color code: Sl, O – brown; C_{12} – red; C_{14} – pink; C_{16} – black; C_{18} – grey; TMS – purple; silanol – yellow; toluene – green.

exclusion effect of a cylindrical pore model with a diameter of 28 Å relative to a pore model with a diameter of 66 Å. Fig. 9 illustrates the larger pore model, including the attached reservoir region.[83]

Simulations of mixtures containing 1-dodecene, 1-tetradecene, 1-hexadecene and 1-octadecene molecules showed differences in the probability of pore occupancy. While in the larger pore all species are present, the smaller pore hardly hosts C_{18} chains and few C_{16} and C_{14} chains. The C_{12} chain has the highest probability to be accommodated inside the pore (Fig. 10). This supports the concept of steric confinement in that it suggests that the stability of large chromacycles decreases with decreasing pore diameter, too. Simulations containing only a single species confirm this observation, see Fig. S25.

Conclusions

This work extends the scant literature on ethylene oligomerization catalyzed by Cr(II) and Cr(III) catalysts immobilized inside small mesopores. Characterization data and experimental results revealed that the chromium catalysts can be selectively immobilized inside the mesopores of different OMS materials. The pore diameter strongly affects catalytic performance. EXAFS analysis was employed to explore the bonding environment around chromium in different immobilized Cr species. In comparison to the homogeneous catalysts, upon activation with MAO, the supported chromium complexes experienced a clear confinement effect. Catalysts **Cr1@OMS$_{28Å}$**/MAO and **Cr2@OMS$_{28Å}$**/MAO immobilized inside well-defined small mesopores demonstrated the ability to generate lower linear α-olefins up to C_{12} with high selectivity. The confinement provided by the small mesopores was further explored using MD simulations. Our approach provides a convenient probe for confinement imparted by enclosing the chromium active sites within the small mesopores and offers the possibility to tailor the oligomerization selectivity towards LAOs ≤ C_{12}, suppressing PE formation at the same time.

Experimental

General

All reactions were performed under the exclusion of air and moisture by standard Schlenk techniques unless noted otherwise. Reactions involving Cr-complexes were performed in a nitrogen-filled glove box (MBraun Labmaster 130). Glassware was either stored at 120 °C overnight and cooled in an evacuated antechamber or dried at 500 °C under high vacuum (0.01 mbar). ^{1}H- and ^{13}C-NMR spectra were recorded on a Bruker Avance III 400 spectrometer at 400 and 101 MHz, respectively. Chemical shifts are reported in ppm from tetramethylsilane with the solvent resonance resulting from residual solvent protons ($CDCl_3$: 7.26 ppm, C_6D_6: 7.15 ppm, CD_2Cl_2: 5.13 ppm) as reference. Data are reported as follows: chemical shift, multiplicity (s = singlet, d = doublet, t = triplet, pst = pseudo triplet, q = quartet, quint = quintet, sept = septet, br = broad, m = multiplet), integral and coupling constants (Hz). Differential scanning calorimetry (DSC) was

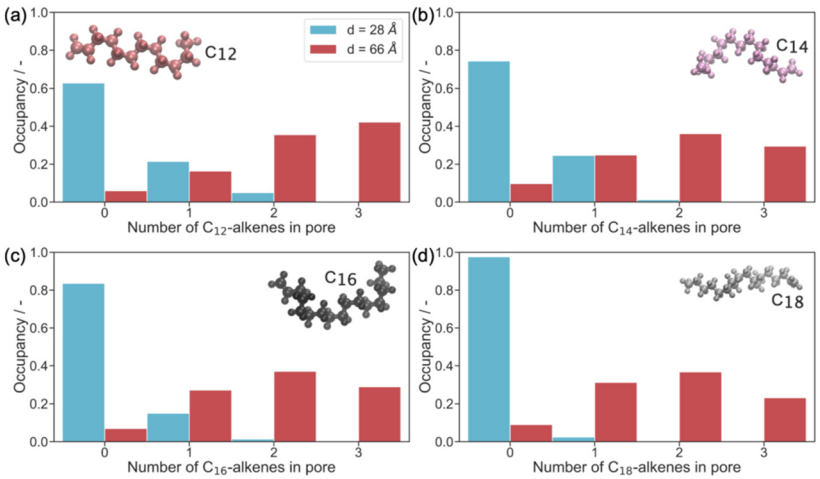

Fig. 10 Frequency of occupancy of 1-alkenes in 28 Å and 66 Å pores observed in simulations of 1-alkene mixtures. (a) C_{12}, (b) C_{14}, (c) C_{16} and (d) C_{18}.

carried out on a PerkinElmer DSC 4000 equipped with a PerkinElmer Intracooler 2p Cryostat. Data were analyzed with the Pyris software. Approximately 8–20 mg of each polymer sample were crimped in aluminum pans for each run. Samples were heated from −50 °C to 200 °C at a rate of 10 °C min^{-1} and then cooled at the same rate. The heating and cooling steps were repeated twice. T_m values were determined from the middle point of the phase transition of the second heating scan. Inductively-coupled plasma-optical emission spectrometry (ICP-OES) measurements were carried out on an Agilent 7500a ICP-OES instrument. For analysis, the corresponding silica (25–35 mg) was mixed with aqua regia (*ca.* 5 g) and water (*ca.*1 g) and then subjected to microwave digestion using a model CEM Mars 6 microwave reaction system. PTFE-TFM vessels (MF 100) were used to digest the samples at 200 °C with 15 min ramp up temperature, at a maximum power of 1000 W for 1 h. After cooling (15 min), the digested samples were syringe-filtered and transferred to a volumetric flask and diluted to 50 mL using deionized ultra-pure water. Cr was measured at λ = 240.272 nm, the background was measured at λ_1 = 240.223–240.254 nm and λ_2 = 240.295–240.340 nm, respectively. The limit of detection (LOD) was 0.0001 mg L^{-1}. For calibration, aqueous Cr-standards with Cr concentrations of 0.000, 0.100, 0.500, 1.000, 2.500 and 5.000 mg L^{-1} were used. For comparison, a reference, containing the same amount of aqua regia and deionized water was subjected to the same treatment. GC–MS analyses were performed on an Agilent Technologies 5975 C inert MSD device consisting of a triple-axis detector, a 7693 autosampler and a 7890 A GC system equipped with an SPB-5 fused silica column (34.13 m × 0.25 mm × 0.25 μm film thickness). GC data were plotted in Excel (Microsoft). *n*-Dodecane together with 1-hexene, 1-octene, 1-decene, 1-dodecene, 1-tetradecene, 1-hexadecene, and 1-octadecene, was used as the internal standard. Selectivity for linear α-olefins was defined as the ratio of linear α-olefins of all fractions over the total amount of oligomer products in percent. XAS samples were measured at the chromium K-edge (5989 eV) in fluorescence (**Cr1@OMS$_{66Å}$, Cr2@OMS$_{57Å}$** and **Cr3@OMS$_{66Å}$** and **Cr3_MAO activated**) and transmission (**Cr1**, **Cr2**, **Cr3** and **Cr(0)(benzene)$_2$**) mode at the P65 beamline (PETRA III, DESY). Measurements were carried out at room temperature up to 1000 eV above the Cr K-edge. I_0 was detected using an ionization chamber filled with 1000 mbar of N_2, I_f used for analyzing the immobilized samples was collected with a PIPS detector located orthogonal to the incident X-ray beam. For the analysis of the homogeneous samples, I_1 was detected using an ionization chamber filled with 910 mbar of N_2 plus 90 mbar of Ar. In the fluorescence mode, the samples were tilted by 45 degrees relative to this beam. For energy selection, a Si(111) double crystal monochromator (DCM) was used with a resolving power of 1–2 × 10^{-4} resulting in an averaged experimental resolution at Cr K-edge of app. 1 eV. For energy calibration, a chromium foil was measured before and after the chromium samples. Quantification of the absorption edge energy E_0 was performed by identifying the first inflection point in the XANES spectrum of the chromium foil. The immobilized samples were measured without any additive binder to not further decrease the concentration of the chromium centers, the homogeneous solid samples were mixed with dry boron nitride. The concentration was calculated for an edge jump of 0.3. Spectra showing beginning radiation damage were not included in the data analysis. **Cr1@OMS$_{28Å}$, Cr2@OMS$_{28Å}$** and **Cr3@OMS$_{28Å}$** as well as immobilized MAO-activated species could not be investigated due to either insufficient signal quality or rapid photodecomposition. XANES- and EXAFS-analysis of the experimental spectra was accomplished with the aid of the Demeter package.[84] Background subtraction and normalization of the XAS raw data were performed with the Athena software. EXAFS fitting was carried out using the Artemis software applying the full multiple scattering approach (FMS).[85] During the multiple parameter EXAFS fitting procedure, the parameters for each sample were set individually. N_2-physisorption analyses were performed at 77 K on a Quantachrome QuadraSorb automatic volumetric instrument. Silica samples were degassed for 11 h at 150 °C *in vacuo* prior to the gas adsorption studies. Pore size distributions, pore volumes and surface areas were calculated from the desorption branch using the non-local density functional theory (NLDFT) cylindrical adsorption pores for silica implemented in the ASiQwin software version 3.01. Toluene was dried with an MBraun SPS-800 solvent purification system with alumina drying columns and stored over 4 Å Linde type molecular sieves. Deuterated solvents were filtered over activated alumina and stored over 4 Å Linde type molecular sieves inside the glove box. All catalyst preparations were carried out in oven-treated glassware. $CrCl_3(THF)_3$ was purchased from ABCR Chemicals. $CrCl_2$ was purchased from Sigma-Aldrich. MAO (10 wt% in toluene) was sourced from Sigma-Aldrich, toluene was removed *in vacuo* at 60 °C, and MAO was obtained as a white semi-crystalline powder and used as a cocatalyst in ethylene oligomerization. Si60 was purchased from Machery-Nagel Gmbh & Co. KG, residual moisture was removed under vacuum at 200 °C overnight and stored inside the glovebox. OMS materials were synthesized *via* a true liquid crystal templating process as described previously.[36,86]

General procedure for catalytic ethylene oligomerization

Ethylene oligomerization was performed in a 250 mL stainless steel reactor (Berghof, type 25) equipped with a mechanical stirrer and a thermostat. The catalyst (*ca.* 1 mg) or the supported catalyst (*ca.* 15 mg), cocatalyst MAO (1000 eq.), toluene (10 mL) and internal standard dodecane (50 μL) were transferred to the fully dried reactor under a nitrogen atmosphere. The reactor was immediately charged with ethylene to the desired pressure and the reaction temperature was controlled by using a thermostat. After the reaction

mixture was stirred for the desired period, the pressure was released and the reactor was cooled in an ice bath. The reaction mixture was quenched with water (5 mL) and MTBE (3 mL) was added subsequently. A small sample of the upper-layer solution was filtered through a syringe filter and analyzed by GC for determining the composition and mass distribution of oligomers obtained. Then the residual reaction solution was quenched with 5% hydrochloric acid in ethanol. The remainder of the organic layer was filtered to isolate the precipitated polymeric material, which was dried in an oven at 80 °C overnight and weighed. Each catalytic test was performed at least twice to ensure reproducibility of the results. The Al : Cr ratio used was 1000 : 1 unless stated otherwise.

Modification of ordered mesoporous silica ($OMS_{28Å}$, $OMS_{57Å}$, and $OMS_{66Å}$)[47]

Refilling of OMS – OMS material (approx. 10 g) was added to a solution of terpolymer (Pluronic® P-123, 40 g) in ethanol (150 mL) and the suspension was stirred for 24 h at room temperature. The suspension was filtered and dried *in vacuo* at 80 °C for 24 h.

Selective protection of silanol groups outside the mesopores – the refilled OMS (approx. 15 g) was stirred in hexamethyldisilazane (200 mL) for 3 h at room temperature, filtered and washed with hexane (500 mL).

Removal of the surfactant – P123 was removed by Soxhlet extraction with ethanol at 140 °C for 168 h.

Immobilization of catalyst

Refilled, selectively protected, and extracted silica (100 mg) was added to a solution of the catalyst (5 mg) in toluene (3 mL). For the removal of nitrogen in the pores, low vacuum (*ca.* 500 mbar) was applied. The suspension was stirred for 16 h at room temperature. Then, the suspension was filtered and the resulting silica containing the immobilized catalyst was washed with toluene (150 mL), dichloromethane (50 mL) and *n*-pentane (150 mL), dried under vacuum at room temperature for several hours and stored under inert atmosphere at −35 °C.

Author contributions

Somnath Bhattacharya: formal analysis, investigation, data curation, writing – original draft. Marc Högler: investigation, formal analysis. Johanna R. Bruckner: resources. Boshra Atwi: formal analysis. Niels Hansen: methodology, writing – review and editing. Matthias Bauer: methodology, writing – review and editing. Felix R. Fisher: investigation, formal analysis, writing – original draft. Michael R. Buchmeiser: conceptualization, project administration, funding acquisition, supervision, writing – review and editing. The manuscript was written through contributions of all authors. All authors have given approval to the final version of the manuscript.

Conflicts of interest

There are no conflicts to declare.

Data availability

Supplementary information (SI) available: all experimental data supporting the findings of this contribution (^{1}H and ^{13}C NMR spectra of all ligands and PE, GC–MS spectra, ICP–OES data, BET data, DSC data, MD simulations and XANES and EXAFS data) (PDF). See DOI: https://doi.org/10.1039/d5cy01483b.

Acknowledgements

This work was supported by the Deutsche Forschungsgemeinschaft DFG (project no. 358283783 - SFB1333/2 2022) and the Ministry of Science, Research and the Arts Baden-Württemberg (Margarete von Wrangell program, Johanna R. Bruckner). Beamline P65 of PETRA III at DESY is kindly acknowledged for provision of beamtime. For measurements, we like to thank Dr. Patrick Probst and Sarthak Mohanty (ICP–OES), and Dr. Dongren Wang (^{13}C NMR measurements of PE) for help and support.

References

1 D. Vogt, in *Applied Homogeneous Catalysis with Organometallic Compounds: a Comprehensive Handbook*, Wiley-VCH, Weinheim, Germany, 2nd edn, 2002, vol. 1, pp. 240–253.
2 F. J. Karol, G. L. Karapinka, C. Wu, A. W. Dow, R. N. Johnson and W. L. Carrick, *J. Polym. Sci., Part A-1: Polym. Chem.*, 1972, **10**, 2621–2637.
3 Q. Lo, D. Pye, S. Gesslbauer, Y. Sim, F. García, A. J. White and G. J. Britovsek, *Catal. Sci. Technol.*, 2022, **12**, 4544–4551.
4 S. Peitz, B. R. Aluri, N. Peulecke, B. H. Müller, A. Wöhl, W. Müller, M. H. Al-Hazmi, F. M. Mosa and U. Rosenthal, *Chem. – Eur. J.*, 2010, **16**, 7670–7676.
5 S. Härzschel, F. E. Kühn, A. Wöhl, W. Müller, M. H. Al-Hazmi, A. M. Alqahtani, B. H. Müller, N. Peulecke and U. Rosenthal, *Catal. Sci. Technol.*, 2015, **5**, 1678–1682.
6 B. L. Small, *Acc. Chem. Res.*, 2015, **48**, 2599–2611.
7 C. Bariashir, C. Huang, G. A. Solan and W.-H. Sun, *Coord. Chem. Rev.*, 2019, **385**, 208–229.
8 J. Petit, L. Magna and N. Mézailles, *Coord. Chem. Rev.*, 2022, **450**, 214227.
9 O. L. Sydora, *Organometallics*, 2019, **38**, 997–1010.
10 M. J. Overett, K. Blann, A. Bollmann, J. T. Dixon, D. Haasbroek, E. Killian, H. Maumela, D. S. McGuinness and D. H. Morgan, *J. Am. Chem. Soc.*, 2005, **127**, 10723–10730.
11 G. J. Britovsek, D. S. McGuinness, T. S. Wierenga and C. T. Young, *ACS Catal.*, 2015, **5**, 4152–4166.
12 D. S. McGuinness, V. C. Gibson, D. F. Wass and J. W. Steed, *J. Am. Chem. Soc.*, 2003, **125**, 12716–12717.
13 J. Zhang, X. Wang, X. Zhang, W. Wu, G. Zhang, S. Xu and M. Shi, *ACS Catal.*, 2013, **3**, 2311–2317.

14 X. Zhao, J. Wang, D. Liu, W. Kong and J. Zhang, *ACS Omega*, 2023, **8**, 34549–34556.
15 D. S. McGuinness, *Chem. Rev.*, 2011, **111**, 2321–2341.
16 D. S. McGuinness, P. Wasserscheid, W. Keim, D. Morgan, J. T. Dixon, A. Bollmann, H. Maumela, F. Hess and U. Englert, *J. Am. Chem. Soc.*, 2003, **125**, 5272–5273.
17 D. S. McGuinness, P. Wasserscheid, W. Keim, C. Hu, U. Englert, J. T. Dixon and C. Grove, *Chem. Commun.*, 2003, 334–335.
18 D. S. McGuinness, J. A. Suttil, M. G. Gardiner and N. W. Davies, *Organometallics*, 2008, **27**, 4238–4247.
19 J. Peng, Y. Mei, L. Chen, M. Zhu and Z. Liu, *J. Catal.*, 2024, **429**, 115279.
20 T. Agapie, *Coord. Chem. Rev.*, 2011, **255**, 861–880.
21 S. Kuhlmann, J. T. Dixon, M. Haumann, D. H. Morgan, J. Ofili, O. Spuhl, N. Taccardi and P. Wasserscheid, *Adv. Synth. Catal.*, 2006, **348**, 1200–1206.
22 A. Peng, Z. Huang and G. Li, *Catalysts*, 2024, **14**, 268.
23 M. Lamb, D. Apperley, M. Watson and P. Dyer, *Top. Catal.*, 2018, **61**, 213–224.
24 M. L. Shozi, X. Zulu and H. B. Friedrich, *S. Afr. J. Chem.*, 2021, **75**, 32–39.
25 X. Gao, M. Wang, Y. Chen, Y. Sun, B. Dong and T. Jiang, *React. Kinet., Mech. Catal.*, 2014, **113**, 159–167.
26 T. Müller, J. T. Dixon, M. Haumann and P. Wasserscheid, *React. Chem. Eng.*, 2019, **4**, 131–140.
27 M. Fallahi, E. Ahmadi, A. Ramazani and Z. Mohamadnia, *J. Organomet. Chem.*, 2017, **848**, 149–158.
28 S. Liu, Y. Zhang, Y. Han, G. Feng, F. Gao, H. Wang and P. Qiu, *Organometallics*, 2017, **36**, 632–638.
29 T. A. Goetjen, X. Zhang, J. Liu, J. T. Hupp and O. K. Farha, *ACS Sustainable Chem. Eng.*, 2019, **7**, 2553–2557.
30 D. F. Wass, *US Pat.*, US6800702B2, 2002.
31 T. Monoi and Y. Sasaki, *J. Mol. Catal. A: Chem.*, 2002, **187**, 135–141.
32 C. N. Nenu and B. M. Weckhuysen, *Chem. Commun.*, 2005, 1865–1867.
33 H. Shao, H. Zhou, X. Guo, Y. Tao, T. Jiang and M. Qin, *Catal. Commun.*, 2015, **60**, 14–18.
34 Y. Habibi, M. Marefat, S. Gharajedaghi, M. Mohamadhoseini, Z. Mohamadnia and E. Ahmadi, *Sci. Rep.*, 2025, **15**, 1–14.
35 F. Ziegler, J. Teske, I. Elser, M. Dyballa, W. Frey, H. Kraus, N. Hansen, J. Rybka, U. Tallarek and M. R. Buchmeiser, *J. Am. Chem. Soc.*, 2019, **141**, 19014–19022.
36 F. Ziegler, H. Kraus, M. J. Benedikter, D. Wang, J. R. Bruckner, M. Nowakowski, K. Weißer, H. Solodenko, G. Schmitz and M. Bauer, *ACS Catal.*, 2021, **11**, 11570–11578.
37 F. Ziegler, J. R. Bruckner, M. Nowakowski, M. Bauer, P. Probst, B. Atwi and M. R. Buchmeiser, *ChemCatChem*, 2023, **15**, e202300871.
38 M. Nandeshwar, K. Weisser, F. Ziegler, W. Frey and M. R. Buchmeiser, *ChemCatChem*, 2025, **17**, e202401561.
39 P. K. Panyam and M. R. Buchmeiser, *Faraday Discuss.*, 2023, **244**, 39–50.
40 B. Atwi, D. Wang, J. R. Bruckner, W. Frey and M. R. Buchmeiser, *Catal. Sci. Technol.*, 2025, **15**, 7059–7066.
41 S. Bhattacharya, B. Atwi, K. Kundu, W. Frey and M. R. Buchmeiser, *Organometallics*, 2025, **44**, 315–324.
42 S. Bhattacharya, F. Ziegler, D. Wang, W. Frey and M. R. Buchmeiser, *Organometallics*, 2024, **43**, 677–688.
43 C. Müller, D. M. Andrada, I.-A. Bischoff, M. Zimmer, V. Huch, N. Steinbrück and A. Schäfer, *Organometallics*, 2019, **38**, 1052–1061.
44 P. P. Samuel, R. Neufeld, K. C. Mondal, H. W. Roesky, R. Herbst-Irmer, D. Stalke, S. Demeshko, F. Meyer, V. C. Rojisha and S. De, *Chem. Sci.*, 2015, **6**, 3148–3153.
45 S. P. Varkey, R. F. Lobo and K. H. Theopold, *Catal. Lett.*, 2003, **88**, 227–229.
46 H. Shao, Y. Li, X. Gao, C. Cao, Y. Tao, J. Lin and T. Jiang, *J. Mol. Catal. A: Chem.*, 2014, **390**, 152–158.
47 P. Probst, M. Lindemann, J. R. Bruckner, B. Atwi, D. Wang, F. R. Fischer, M. Högler, M. Bauer, N. Hansen, M. Dyballa and M. R. Buchmeiser, *J. Am. Chem. Soc.*, 2025, **147**, 8741–8750.
48 M. Thommes, K. Kaneko, A. V. Neimark, J. P. Olivier, F. Rodriguez-Reinoso, J. Rouquerol and K. S. W. Sing, *Pure Appl. Chem.*, 2015, **87**, 1051–1069.
49 M. Bauer and H. Bertagnolli, in *Methods in Physical Chemistry*, Wiley-VCH, Weinheim, Germany, 2012, vol. 10, pp. 231–269.
50 M. Tromp, *Philos. Trans. R. Soc., A*, 2015, **373**, 20130152.
51 L. Burkhardt, M. Holzwarth, B. Plietker and M. Bauer, *Inorg. Chem.*, 2017, **56**, 13300–13310.
52 L. Burkhardt, Y. Vukadinovic, M. Nowakowski, A. Kalinko, J. Rudolph, P.-A. Carlsson, C. R. Jacob and M. Bauer, *Inorg. Chem.*, 2020, **59**, 3551–3561.
53 M. Tromp, J. Moulin, G. Reid and J. Evans, *AIP Conf. Proc.*, 2007, **882**, 699–701.
54 M. Bauer, U. Bentrup, J. Priebe and A. Brückner, in *Contemporary Catalysis: Science, Technology, and Applications*, RSC, Cambridge, 2017, pp. 549–588.
55 D. Trummer, K. Searles, A. Algasov, S. A. Guda, A. V. Soldatov, H. Ramanantoanina, O. V. Safonova, A. A. Guda and C. Copéret, *J. Am. Chem. Soc.*, 2021, **143**, 7326–7341.
56 A. Pantelouris, H. Modrow, M. Pantelouris, J. Hormes and D. Reinen, *Chem. Phys.*, 2004, **300**, 13–22.
57 S. Conde-Guadano, M. Hanton, R. P. Tooze, A. A. Danopoulos and P. Braunstein, *Dalton Trans.*, 2012, **41**, 12558–12567.
58 A. Trivedi, M. A. Alam, A. Khooha, R. Dhawan, R. K. Sharma, S. Tripathi and M. K. Tiwari, *Surf. Interface Anal.*, 2024, **56**, 760–769.
59 P. Glatzel, G. Smolentsev and G. Bunker, *J. Phys.: Conf. Ser.*, 2009, **190**, 012046.
60 J. Yi, N. Nakatani, K. Nomura and M. Hada, *Phys. Chem. Chem. Phys.*, 2020, **22**, 674–682.
61 T. Yokoyama, N. Kosugi and H. Kuroda, *Chem. Phys.*, 1986, **103**, 101–109.
62 R. A. Bair and W. A. Goddard III, *Phys. Rev. B*, 1980, **22**, 2767.
63 J. Yi, N. Nakatani and K. Nomura, *Dalton Trans.*, 2020, **49**, 8008–8028.

64 R. Grauke, R. Schepper, J. Rabeah, R. Schoch, U. Bentrup, M. Bauer and A. Brückner, *ChemCatChem*, 2020, **12**, 1025–1035.
65 J. Rabeah, M. Bauer, W. Baumann, A. E. McConnell, W. F. Gabrielli, P. B. Webb, D. Selent and A. Brückner, *ACS Catal.*, 2013, **3**, 95–102.
66 K. P. Bryliakov, N. V. Semikolenova, V. N. Zudin, V. A. Zakharov and E. P. Talsi, *Catal. Commun.*, 2004, **5**, 45–48.
67 B. Venderbosch, L. A. Wolzak, J.-P. H. Oudsen, B. De Bruin, T. J. Korstanje and M. Tromp, *Catal. Sci. Technol.*, 2020, **10**, 6212–6222.
68 B. Venderbosch, J.-P. H. Oudsen, L. A. Wolzak, D. J. Martin, T. J. Korstanje and M. Tromp, *ACS Catal.*, 2018, **9**, 1197–1210.
69 T. W. Hey and D. F. Wass, *Organometallics*, 2010, **29**, 3676–3678.
70 M. Ngcobo, A. Ouissa, W. Kleist, W. R. Thiel and S. O. Ojwach, *Mol. Catal.*, 2023, **549**, 113465.
71 F. Alam, J. Wang, C. Dong, Q. Chang, L. Zhang, Q. Zhang, Y. Chen and T. Jiang, *J. Catal.*, 2020, **392**, 278–286.
72 L. Guo, Y. Zhang, W. Chen, Y. Li, D. Song, W. Yang, J. Huang, F. Li, C. Li and Z. Guo, *ACS Sustainable Chem. Eng.*, 2025, **13**, 7520–7531.
73 A. N. Mlinar, S. Shylesh, O. C. Ho and A. T. Bell, *ACS Catal.*, 2014, **4**, 337–343.
74 D. Cicmil, I. Van Ravenhorst, J. Meeuwissen, A. Vantomme and B. Weckhuysen, *Catal. Sci. Technol.*, 2016, **6**, 731–743.
75 G. A. Martino, A. Piovano, C. Barzan, J. Rabeah, G. Agostini, A. Bruekner, G. Leone, G. Zanchin, T. Monoi and E. Groppo, *ACS Catal.*, 2020, **10**, 2694–2706.
76 U. Kanbur, J. N. Hall, Y. L. Kim, J. Niklas, O. G. Poluektov, C. Liu, A. J. Kropf, M. Delferro and D. M. Kaphan, *ACS Catal.*, 2024, **14**, 8640–8651.
77 J. Dai and H. Zhang, *Small*, 2021, **17**, 2005334.
78 V. Mouarrawis, R. Plessius, J. I. Van der Vlugt and J. N. Reek, *Front. Chem.*, 2018, **6**, 623.
79 H. Toulhoat, M. Lontsi Fomena and T. de Bruin, *J. Am. Chem. Soc.*, 2011, **133**, 2481–2491.
80 H. Shao, J. Wang, R. Wang, L. Song, X. Guo and T. Jiang, *Appl. Catal., A*, 2017, **544**, 154–160.
81 H. Xu and C.-Y. Guo, *Eur. Polym. J.*, 2015, **65**, 15–32.
82 M. P. McDaniel, *J. Catal.*, 2009, **261**, 34–49.
83 H. Kraus, J. Rybka, A. Höltzel, N. Trebel, U. Tallarek and N. Hansen, *Mol. Simul.*, 2021, **47**, 306–316.
84 B. Ravel and M. Newville, *J. Synchrotron Radiat.*, 2005, **12**, 537–541.
85 J. J. Rehr, J. J. Kas, F. D. Vila, M. P. Prange and K. Jorissen, *Phys. Chem. Chem. Phys.*, 2010, **12**, 5503–5513.
86 J. R. Bruckner, J. Bauhof, J. Gebhardt, A.-K. Beurer, Y. Traa and F. Giesselmann, *J. Phys. Chem. B*, 2021, **125**, 3197–3207.
87 S. Bhattacharya, M. Högler, J. R. Bruckner, B. Atwi, N. Hansen, F. R. Fischer and M. R. Buchmeiser, *ChemRxiv*, 2025, preprint, DOI: 10.26434/chemrxiv-2025-kwldf.